Ultrasonics - Sonochemistry 56 (2019) 14–24

Contents lists available at ScienceDirect

Ultrasonics - Sonochemistry

journal homepage: www.elsevier.com/locate/ultson

Fast and simultaneous doping of $Sr_{0.9-x-y-z}Ca_{0.1}In_2O_4$:($xEu^{3+}$, yTm^{3+}, zTb^{3+}) superstructure by ultrasonic spray pyrolysis

A.A.G. Santiago[a,*], L.X. Lovisa[a], P.N. Medeiros[b], M.S. Li[c], N.L.V. Carreño[d], E. Longo[e], C.A. Paskocimas[a], M.R.D. Bomio[a], F.V. Motta[a]

[a] LSQM, DEMAT, UFRN, Natal, Campus Lagoa Nova, CEP 59078-900 Natal, RN, Brazil
[b] IFBA, Instituto Federal da Bahia – Campus Jacobina, 44700-000 Jacobina, BA, Brazil
[c] IFSC, USP, Av. Trabalhador São Carlense, 400, CEP 13566-590 São Carlos, SP, Brazil
[d] Graduate Program in Materials Science and Engineering, Technology Development Center, Federal University of Pelotas, 96010-000 Pelotas, RS, Brazil
[e] LIEC, DQ, UFSCar, CEP 13565-905 São Carlos, SP, Brazil

ARTICLE INFO

Keywords:
Ultrasonic spray pyrolysis
Photoluminescence
Strontium indate
Europium
Terbium
Thulium

ABSTRACT

In the present work, $Sr_{0.9-x-y-z}Ca_{0.1}In_2O_4$:($xEu^{3+}$, yTm^{3+}, zTb^{3+}) particles were synthesized by the ultrasonic spray pyrolysis (USP) method to obtain a single-phase white phosphorus formed by six different cations in solution within the lattice (superstructure). The samples were also structurally and morphologically characterized by X-ray diffraction (XRD) techniques and by field emission scanning electron microscopy (FE-SEM). The photoluminescent behavior and the characteristics of the emitted colors were studied by the variation in the co-doping of the rare earth elements. The $Sr_{0.9}Ca_{0.1}In_2O_4$ sample showed a near blue color emission, but all co-doped samples showed emission in white with very close chromaticity coordinates to the standard white (x = 0.33 and y = 0.33). The $Tm^{3+} \rightarrow Tb^{3+}$ (ET1), $Tm^{3+} \rightarrow Eu^{3+}$ (ET2) and $Tb^{3+} \rightarrow Eu^{3+}$ (ET3) Energy Transfers were proposed and are considered necessary for adjusting and controlling the desired color properties.

1. Introduction

$SrIn_2O_4$ is a semiconductor that presents several applications in the area of photoluminescence [1,2] and photocatalysis [3,4]. The properties presented by $SrIn_2O_4$ are related to the structural arrangement of the clusters [InO_6] [5]. In the structure of $SrIn_2O_4$, the distorted octahedra [InO_6] are connected by sharing their edges and angles, and have eight coordinated Sr atoms [6], showing an orthorhombic $CaFe_2O_4$ structure with a $PnamD_{2h}^{16}$ space group [7].

$SrIn_2O_4$ is considered an efficient host network for rare earth ions because of its physico-chemical stability and low phonon energy (467 cm^{-1}) [8]. The use of rare earth (RE) ions as dopants in the $SrIn_2O_4$ matrix enables enhancing the photoluminescent characteristics of the material. The new spectroscopic properties and various applications involving the use of RE were identified [9–13].

The generation of white light has been the target of several studies due to its great potential for applications in exposure and lighting [14–16]. The use of an inorganic host matrix coded with different rare earth ions which present different specific electronic transitions in the visible region has been highlighted by the results [17,18]. The success in developing these materials is related to the production of white light emitting phosphors based on the energy transfer mechanism from the sensitizer to the activator [19,20]. Some host matrices can act as a sensitizer. To do so, it is necessary to utilize different synthesis methods and to observe the obtained physicochemical and thermochemical properties in order to guarantee good performance [21–23].

Ultrasonic pyrolysis spray (USP) method consists of atomizing or nebulizing a precursor solution by an ultrasonic transducer, then the droplets undergo different and simultaneous physicochemical phenomena when subjected to the thermal treatment. These phenomena may include solvent evaporation, precipitation and drying of the solutes, decomposition, chemical alteration through reduction or oxidation, resulting in the formation of fine powders with morphology of non-agglomerated microspheres [24–26].

The luminescent property of the materials arises from the complex interaction between the host matrix, the activating ions (RE^{3+} = Eu^{3+}, Tm^{3+}, Tb^{3+}) and the structural and electronic flaws. This work can be considered a continuation of the "Influence Ca-doped $SrIn_2O_4$ powders on photoluminescence property prepared by ultrasonic spray pyrolysis" [27], in which doping with 10% Ca in $SrIn_2O_4$ obtained good photoluminescent properties. Thus, the purpose of this study is to evaluate the influence of $Sr_{0.9-x-y-z}Ca_{0.1}In_2O_4$:($xEu^{3+}$, yTm^{3+}, zTb^{3+}) as a

* Corresponding author.
E-mail address: andersonsantiago@ufrn.edu.br (A.A.G. Santiago).

https://doi.org/10.1016/j.ultsonch.2019.03.028
Received 31 August 2018; Received in revised form 18 February 2019; Accepted 27 March 2019
Available online 28 March 2019

Table 1
The samples codes table $Sr_{0.9-x-y-z}Ca_{0.1}In_2O_4$:($xEu^{3+}$, yTm^{3+}, zTb^{3+} % mol).

x	y	z	Code
0%	0%	0%	SCIO
1%	1%	1%	SCIO-1.0RE
1.5%	1%	1%	SCIO-1.5Eu
2%	1%	1%	SCIO-2.0Eu
1%	1.5%	1%	SCIO-1.5Tm
1%	2%	1%	SCIO-2.0Tm
1%	1%	1.5%	SCIO-1.5Tb
1%	1%	2%	SCIO-2.0Tb

function of the RE^{3+} concentration variation on the photoluminescent behavior using the following characterization techniques: X-Ray Diffraction (XRD), UV–Visible Spectroscopy, Photoluminescence (PL) and Field Scanning Electron Microscopy (FE-SEM).

2. Experimental

2.1. Materials

First, $Sr_{0.9-x-y-z}Ca_{0.1}In_2O_4$:($xEu^{3+}$, yTm^{3+}, zTb^{3+} mol%) powders were synthesized by the ultrasonic spray pyrolysis method (USP) [24,28]. Strontium nitrate [$Sr(NO_3)_2$] (Alfa Aesar, 99% purity), calcium nitrate tetrahydrate [$Ca(NO_3)_2{\cdot}4\ H_2O$] (Synth, 99% purity), indium nitrate [$In(NO_3)_3$] (Alfa Aesar, 99.9% purity), europium oxide [Eu_2O_3] (Alfa Aesar, 99.9% purity), terbium oxide (Tb_4O_7) (Aldrich, 99.9% purity), thulium oxide (Tm_2O_3) (Aldrich, 99.9% purity) and nitric acid (Synth, 65% PA) were used as precursors.

2.2. Experimental procedure

Eu_2O_3, Tb_4O_7 and Tm_2O_3 oxides were dissolved separately in 10 ml of nitric acid to obtain the respective nitrates, because these oxides were insoluble in the reaction medium. In order to obtain $Sr_{0.87}Ca_{0.1}In_2O_4$:(1% Eu^{3+}, 1% Tm^{3+}, 1% Tb^{3+} %mol) the precursor solution was prepared by dissolving 7.83 mmol of strontium nitrate, 0.9 mmol of calcium nitrate, 0.09 mmol of nitrate of ethanol, 0.09 mmol of thulium nitrate, 0.09 mmol of terbium nitrate and 18 mmol of indium nitrate in 190 ml of distilled water. The solvation energy of H_2O molecules in this solution causes fast dissociation of the reagents, i.e. the Sr^{2+}, Ca^{2+} and In^{3+} are solvated by the H_2O and NO_3^- species. It is well known that the Sr atoms coordinate with two NO_3^-, Ca atoms coordinate with four H_2O and two NO_3^-, and In atoms coordinate with three H_2O and three NO_3^- to form distorted octahedral clusters. There is a strong electrostatic attraction between the [Sr/Ca/Eu/Tb/Tm] and In cluster complexes due to their difference in electronic density between them. When the solvent starts to evaporate, the viscosity of water decreases and the mobility of the cluster complex is then favored, considerably increasing the effective rate of collisions between the species in the solution. Moreover, the thermal decomposition occurs directly in the nucleation sites, forcing the crystallization kinetics of the primary crystals (Eq. (1)).

$$0.9 - x - y - zSr(NO_3)_2 + 0.1Ca(NO_3)_2 + 2In(NO_3)_3 + xEu(NO_3)_3 + yTm(NO_3)_3 + zTb(NO_3)_3 + nH_2O_{(l)} \xrightarrow{\Delta} Sr_{0.9-x-y-z}Eu_xTm_yTb_zCa_{0.1}In_2O_4 + nNO_{2(g)} + nH_2O_{(g)} \quad (1)$$

Then, the precursor solution was atomized using an ultrasonic nebulizer (frequency of 2.4 MHz) with a flow of air (3 L min^{-1}) and the heating temperatures were from 700 °C for zone 1 and 1050 °C for zone 2. Reference [27] describes more details on the equipment and technique used. The other precursor solutions were made according to the stoichiometric shown in Table 1.

2.3. Characterizing $Sr_{0.9-x-y-z}Ca_{0.1}In_2O_4$:($xEu^{3+}$, yTm^{3+}, zTb^{3+} % mol) particles

The $Sr_{0.9-x-y-z}Ca_{0.1}In_2O_4$:($xEu^{3+}$, yTm^{3+}, zTb^{3+} %mol) powders were characterized by XRD 7000, 40 kV and 30 mAh XRD, with CuKα (λ = 1.5406 Å), 2θ of 10° to 80° and step speed of 1° min^{-1}. The 2θ range of 10° to 120° and step speed of 0.02° min^{-1} were used for the Rietveld refinement measure. The morphology was analyzed using field emission scanning electron microscopy (FE-SEM, Carl Zeiss, model

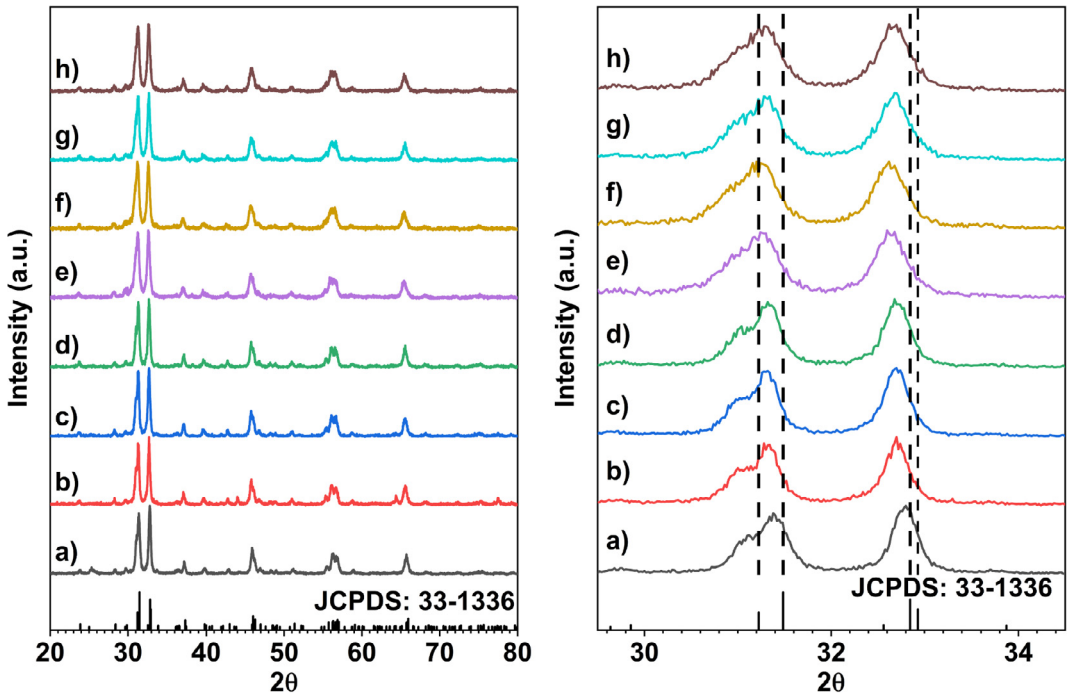

Fig. 1. XRD patterns of $Sr_{0.9-x-y-z}Ca_{0.1}In_2O_4$ obtained by USP (a) SCIO, (b) SCIO-1.0RE, (c) SCIO-1.5Eu, (d) SCIO-2.0Eu, (e) SCIO-1.5Tb, (f) SCIO-2.0Tb, (g) SCIO-1.5Tm and (h) SCIO-2.0Tm.

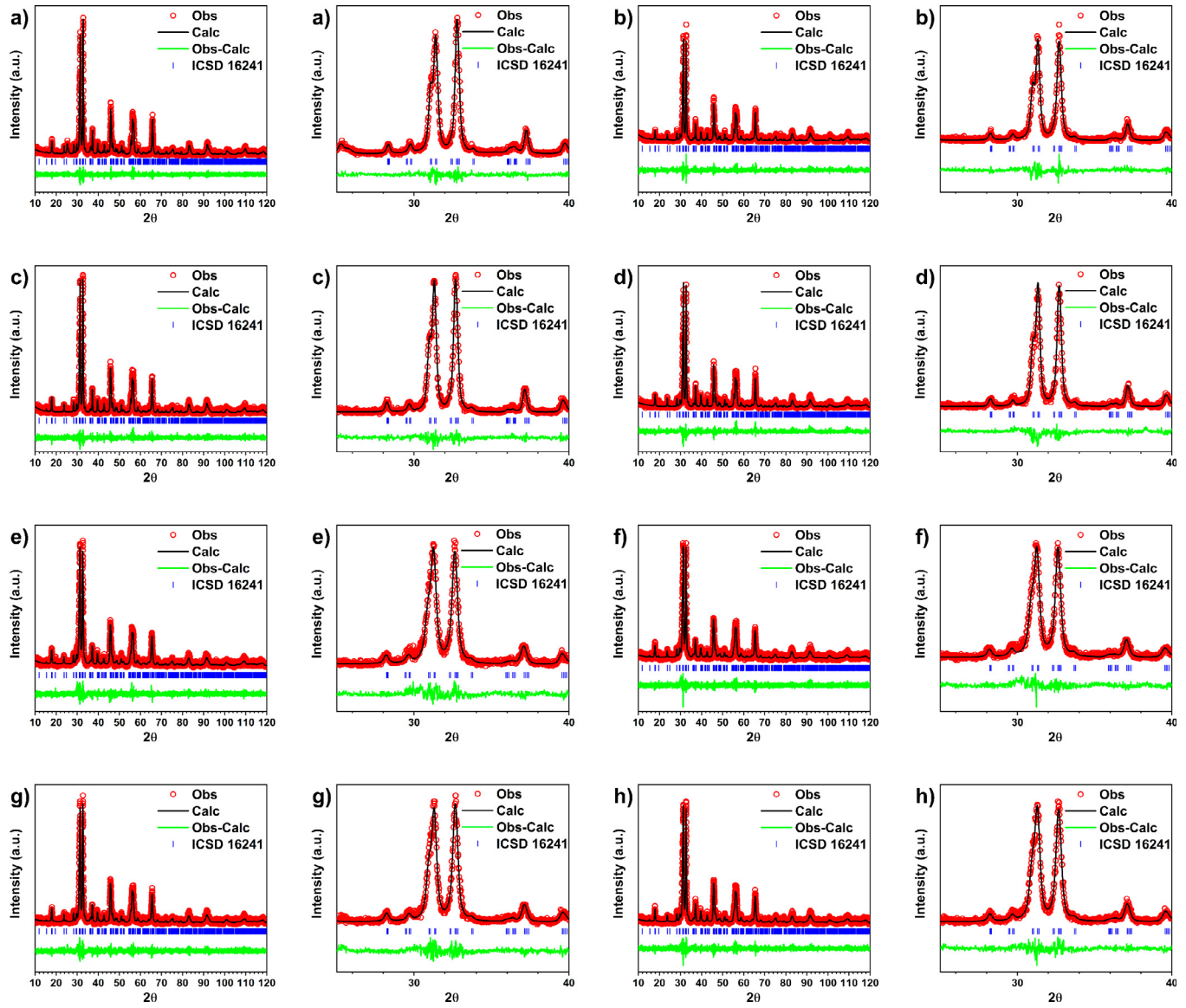

Fig. 2. Rietveld refinement of $Sr_{0.9-x-y-z}Ca_{0.1}In_2O_4$ obtained by USP (a) SCIO, (b) SCIO-1.0RE, (c) SCIO-1.5Eu, (d) SCIO-2.0Eu, (e) SCIO-1.5Tb, (f) SCIO-2.0Tb, (g) SCIO-1.5Tm and (h) SCIO-2.0Tm. Where *Obs* are the experimental data of XRD, *Calc* are the data theoretically calculated to fit the experimental diffractogram, *Obs-Calc* are the difference between the experimental data and calculated data, ICSD 16241 are the bragg peaks of the crystallographic sheet.

Supra 35-VP, operating at 6 kV), the powder of the samples was added in ethanol and dispersed by means of an ultrasonic bath in ethanol for about 10 min, dripped on metal silicon plates and oven dried at 40 °C for 3 h. No metal coating was used on the particles. The UV–Vis reflectance spectrum was obtained using a UV–Vis spectrometer (Shimadzu, model UV-2600). Photoluminescence (PL) spectra were obtained using a Thermal Jarrell-Ash Monospec 27 monochromator and a Hamamatsu R446 photomultiplier. The excitation source used in the samples was a laser with a wavelength of 350.7 nm with krypton ions (Coherent Innova) with an output of approximately 13.3 mW.

3. Results and discussion

3.1. X-ray diffraction

The XRD patterns of $Sr_{0.9-x-y-z}Ca_{0.1}In_2O_4$:($xEu^{3+}$, yTm^{3+}, zTb^{3+} mol%) obtained by the ultrasonic spray pyrolysis method are shown in Fig. 1. The samples were indexed in a unit cell with orthorhombic structure with the *Pnam* (66) space group according to the JCPDS 33-1336. No peaks were observed in the secondary phases of the dopant ions (Ca^{2+}, Eu^{3+}, Tb^{3+} and Tm^{3+}), indicating that the dopant ions were successfully incorporated into the indates structure using the ultrasonic spray pyrolysis method, resulting in forming indices composed of six metal cations. The occurrence of small displacements of diffraction peaks was verified according to the stoichiometry used, which occurs due to the different molarities used in the atomic substitutions of Sr^{2+} ions by of Eu^{3+}, Tb^{3+} and Tm^{3+} ions, resulting in changes in the network parameters of the indate structure.

The Rietveld refinement method [29] using the General Structure Analysis System (GSAS) with graphic interface EXPGUI [30] was used in the XRD patterns of the $Sr_{0.9-x-y-z}Ca_{0.1}In_2O_4$ particles to identify possible modifications in the structures resulting from the different doping. All $Sr_{0.9-x-y-z}Ca_{0.1}In_2O_4$ XRD patterns were indexed as orthorhombic cells (*Pnma*) according to ICSD 16241 ($SrIn_2O_4$). The following parameters were refined: scaling factor and phase fraction; background (displaced Chebyshev polynomial function); peak shape (Thomson-Cox-Hasting pseudo-Voigt); change in the network constants; fractional atomic coordinates; and isotropic thermal parameters. Fig. 2 shows the results obtained from the Rietveld refinement.

As can be seen, the *Obs-Calc* lines of the refinements are tending to

Table 2
Rietveld refined structural parameters for the $Sr_{0.9-x-y-z}Ca_{0.1}In_2O_4$ samples.

Compounds	SCIO	SCIO-1.0RE	SCIO-1.5Eu	SCIO-2.0Eu
Crystal system	Orthorhombic	Orthorhombic	Orthorhombic	Orthorhombic
Space Group	*Pnam*	*Pnam*	*Pnam*	*Pnam*
Lattice parameters (Å)				
a	9.8312	9.8435	9.8474	9.8466
b	11.5089	11.5269	11.5251	11.5264
c	3.2728	3.2792	3.2792	3.2804
α	90°	90°	90°	90°
V(Å³)	370.32	372.08	372.16	372.31
χ^2	1.210	1.364	1.284	1.372
Rwp (%)	17.96	24.91	22.72	23.91
Rp (%)	13.06	18.32	16.27	17.62
D (nm)	31.06	29.97	19.99	21.54
ε (x10⁻³)	1.55	1.01	1.24	1.13
Compounds	SCIO-1.5Tb	SCIO-2.0Tb	SCIO-1.5Tm	SCIO-2.0Tm
Crystal system	Orthorhombic	Orthorhombic	Orthorhombic	Orthorhombic
Space Group	*Pnam*	*Pnam*	*Pnam*	*Pnam*
Lattice parameters (Å)				
a	9.8546	9.8574	9.8493	9.8540
b	11.5482	11.5533	11.5377	11.5407
c	3.2825	3.2844	3.2817	3.2818
α	90°	90°	90°	90°
V(Å³)	373.56	374.04	372.93	373.22
χ^2	1.301	1.302	1.268	1.248
Rwp (%)	22.85	23.00	22.45	22.11
Rp (%)	16.70	16.91	16.46	16.06
D (nm)	13.53	14.22	14.90	13.86
ε (x10⁻³)	1.85	1.77	1.67	1.81

Legend: a, b and *c* = lattice parameters; *α* = angle between *b* and *c*; *V* = unit cell volume; χ^2 = chi-squared; *Rwp* = weighted profile factor; *Rp* = profile factor; *D* = crystallite size; *ε* = microstrain.

be rectilinear, indicating that the differences between the experimental data and the theoretically calculated data are close to zero, showing that the diffraction patterns of the samples are well adapted to ICSD 16241. The results of the structural parameters, atomic positioning and crystallite size of $Sr_{0.9-x-y-z}Ca_{0.1}In_2O_4$ samples are presented in Tables 2 and 3. The reliability parameters *χ2*, *Rwp* and *Rp*, shown in Table 1 indicate good quality of structural refinements and numerical results. The network parameter values, *a*, *b* and *c*, calculated for the samples are values close to those found in the literature. Ming et al [31] obtained $SrIn_2O_4$:0.01Er^{3+} by the solid-state reaction method and the values of the network parameters shown were $a = 9.8317$ Å, $b = 11.4950$ Å and $c = 3.2662$ Å. The SCIO sample showed the following values of network parameters: $a = 9.8312$ Å, $b = 11.5089$ Å and $c = 3.2728$ Å, and the unit cell volume was 370.316 Å³. The small differences observed in the $Sr_{0.9-x-y-z}Ca_{0.1}In_2O_4$ samples and SCIO occurred due to the substitution of Sr^{2+} ions (ionic ratio of 1.260 Å [32]) by Eu^{3+}, Tb^{3+} and Tm^{3+} ions (ionic ratio of 1.066 Å, 1.040 Å and 0.994 Å, respectively [32]) and the different concentrations of each dopant ion. When replacing ions with larger radii by ions with smaller radii, it is expected that the values of the network parameters and consequently the volume of the unit cell decreases [33,34]. In the $Sr_{0.9-x-y-z}Ca_{0.1}In_2O_4$:($x$Eu^{3+}, yTm^{3+}, zTb^{3+}) samples, as shown in Table 2, the unit cell volume values increase as the dopant concentration increases (Eu^{3+}, Tm^{3+} and Tb^{3+}). Bishop et al [35] reported that the phenomenon of network parameter contraction is caused by oxygen vacancies forming due to electrostatic interaction, and the phenomenon of network parameter expansion is due to the change in the cation ratio because of the steric effect. Thus, it is believed that the increase in the network parameters and unit cell volume of $Sr_{0.9-x-y-z}Ca_{0.1}In_2O_4$: ($x$Eu^{3+}, yTm^{3+}, zTb^{3+}) occurs due to the steric effect caused by the valence difference between Sr^{2+} ions and Eu^{3+}, Tb^{3+} and Tm^{3+} ions.

The unit cells of each sample were modeled using the VESTA program [36] from the lattice parameter and atomic coordinate data obtained in the Rietveld refinement (Tables 1 and 2), as shown in Fig. 3.

Table 3
Position of the atoms in the unit cell.

Sample	Atom	x	y	z	Occ
SCIO	Sr1	0.7536	0.6533	0.2500	0.9288
	In1	0.4195	0.1075	0.2500	1.0000
	In2	0.4295	0.6119	0.2500	1.0000
	O1	0.1290	0.1675	0.2500	1.0000
	O2	0.1290	0.4655	0.2500	1.0000
	O3	0.5275	0.7761	0.2500	1.0000
	O4	0.4054	0.4256	0.2500	1.0000
	Ca1	0.7536	0.6533	0.2500	0.1032
SCIO-1.0RE	Sr1	0.7538	0.6519	0.2500	0.8859
	In1	0.4195	0.1081	0.2500	1.0000
	In2	0.4299	0.6119	0.2500	1.0000
	O1	0.2114	0.1634	0.2500	1.0000
	O2	0.1294	0.4744	0.2500	1.0000
	O3	0.5285	0.7834	0.2500	1.0000
	O4	0.4004	0.4134	0.2500	1.0000
	Ca1	0.7538	0.6519	0.2500	0.1017
	Eu1	0.7538	0.6519	0.2500	0.0102
	Tb1	0.7538	0.6519	0.2500	0.0102
	Tm1	0.7538	0.6519	0.2500	0.0102
SCIO-1.5Eu	Sr1	0.7539	0.6522	0.2500	0.8747
	In1	0.4194	0.1077	0.2500	1.0000
	In2	0.4287	0.6120	0.2500	1.0000
	O1	0.2114	0.1592	0.2500	1.0000
	O2	0.1283	0.4807	0.2500	1.0000
	O3	0.5155	0.7886	0.2500	1.0000
	O4	0.4104	0.4231	0.2500	1.0000
	Ca1	0.7539	0.6522	0.2500	0.1010
	Eu1	0.7539	0.6522	0.2500	0.0151
	Tb1	0.7539	0.6522	0.2500	0.0101
	Tm1	0.7539	0.6522	0.2500	0.0101
SCIO-2.0Eu	Sr1	0.7524	0.6527	0.2500	0.8446
	In1	0.4185	0.1087	0.2500	1.0000
	In2	0.4271	0.6120	0.2500	1.0000
	O1	0.2124	0.1793	0.2500	1.0000
	O2	0.1263	0.4739	0.2500	1.0000
	O3	0.5254	0.7873	0.2500	1.0000
	O4	0.4004	0.4171	0.2500	1.0000
	Ca1	0.7524	0.6527	0.2500	0.0982
	Eu1	0.7524	0.6527	0.2500	0.0196
	Tb1	0.7524	0.6527	0.2500	0.0098
	Tm1	0.7524	0.6527	0.2500	0.0098
SCIO-1.5Tb	Sr1	0.7506	0.6498	0.2500	0.8738
	In1	0.4188	0.1081	0.2500	1.0000
	In2	0.4308	0.6104	0.2500	1.0000
	O1	0.2224	0.1644	0.2500	1.0000
	O2	0.1264	0.5034	0.2500	1.0000
	O3	0.5335	0.7874	0.2500	1.0000
	O4	0.4214	0.4108	0.2500	1.0000
	Ca1	0.7506	0.6498	0.2500	0.1009
	Eu1	0.7506	0.6498	0.2500	0.0101
	Tb1	0.7506	0.6498	0.2500	0.0151
	Tm1	0.7506	0.6498	0.2500	0.0101
SCIO-2.0Tb	Sr1	0.7470	0.6506	0.2500	0.8808
	In1	0.4210	0.1085	0.2500	1.0000
	In2	0.4305	0.6118	0.2500	1.0000
	O1	0.2224	0.1494	0.2500	1.0000
	O2	0.1284	0.4934	0.2500	1.0000
	O3	0.5325	0.7934	0.2500	1.0000
	O4	0.4135	0.4112	0.2500	1.0000
	Ca1	0.7470	0.6506	0.2500	0.1023
	Eu1	0.7470	0.6506	0.2500	0.0102
	Tb1	0.7470	0.6506	0.2500	0.0205
	Tm1	0.7470	0.6506	0.2500	0.0102

(*continued on next page*)

Table 3 (*continued*)

Sample	Atom	x	y	z	Occ
SCIO-1.5Tm	Sr1	0.7522	0.6516	0.2500	0.8706
	In1	0.4181	0.1066	0.2500	1.0000
	In2	0.4290	0.6122	0.2500	1.0000
	O1	0.2024	0.1664	0.2500	1.0000
	O2	0.1242	0.4690	0.2500	1.0000
	O3	0.5374	0.7698	0.2500	1.0000
	O4	0.4184	0.4198	0.2500	1.0000
	Ca1	0.7522	0.6516	0.2500	0.1006
	Eu1	0.7522	0.6516	0.2500	0.0101
	Tb1	0.7522	0.6516	0.2500	0.0101
	Tm1	0.7522	0.6516	0.2500	0.0151
SCIO-2.0Tm	Sr1	0.7494	0.6517	0.2500	0.8616
	In1	0.4181	0.1083	0.2500	1.0000
	In2	0.4276	0.6109	0.2500	1.0000
	O1	0.2074	0.1634	0.2500	1.0000
	O2	0.1272	0.4804	0.2500	1.0000
	O3	0.5315	0.7822	0.2500	1.0000
	O4	0.4114	0.4179	0.2500	1.0000
	Ca1	0.7494	0.6517	0.2500	0.1002
	Eu1	0.7494	0.6517	0.2500	0.0100
	Tb1	0.7494	0.6517	0.2500	0.0100
	Tm1	0.7494	0.6517	0.2500	0.0200

The orthorhombic crystal structure (*Pnma*) of strontium indate is formed by two different octahedral clusters of [InO_6] and one octahedron cluster of [SrO_8] [7]. When ionic substitution of the Sr^{2+} atoms by other chemical elements (of the same valence or not) occurs, small distortions happen in the clusters of [InO_6] and [SrO_8] which will result in changes in the atoms positioning of the clusters and changes in the chemical bond length of the atoms inside the unit cell. Schenck and Müller-buschbaum [7] showed that the distance values for a pure sample of $SrIn_2O_4$ between the Sr-O atoms were 2.53 Å (2x), 2.55 Å (2x), 2.61 Å, 2.69 Å, 2.75 Å and 3.76 Å. Fig. 4 shows the [SrO_8]/[CaO_8]/[REO_8] cluster of each $Sr_{0.9-x-y-z}Ca_{0.1}In_2O_4$ sample. It is noted that the substitutions of Sr^{2+} ions by RE^{3+} ions promote distortions in the clusters, resulting in shortening or stretching of Sr-O/Ca-O/RE-O chemical bonds.

3.2. Scanning electron microscopy

Fig. 5 shows the micrographs of the $Sr_{0.9-x-y-z}Ca_{0.1}In_2O_4$ samples obtained by USP. The morphology of $Sr_{0.9-x-y-z}Ca_{0.1}In_2O_4$ samples are formed by slightly distorted microspheres, with the porous surface being similar to a foam. The doped with rare earth elements produced small distortions in the morphology and surface of the microspheres compared to the SCIO sample. It can be seen that the morphology of the pure sample has a spongy shape (Fig. 5a), whereas the doped samples with higher rare earth content have a deflated ball-shape microsphere (Fig. 5d–h). Several physical phenomena occur simultaneously during the Pyrolysis Spray process such as solvent evaporation on the drop's surface, diffusion of solvent vapors away from the drop in the gas phase, drop shrinkage, drop temperature change and solute diffusion in direction to the drop center [37]. In addition to these phenomena, the use of metal nitrates tends to form porous and/or irregular spherical particulates because metal nitrates tend to melt before the solvent is completely removed, forming a molten salt which inhibits solvent removal [37]. Thus, the particles obtained in this study have porous spherical shape due to the use of metallic nitrates in the precursor solution and without large morphological differences among the samples because of the low concentration variation in the rare earth dopants, which does not imply in significant solubility or temperature differences of the nitrate in the percussion solution.

3.3. UV–Visible Spectroscopy

Fig. 6 and Table 4 present the estimated values for the gap energy of $Sr_{0.9-x-y-z}Ca_{0.1}In_2O_4$:($xEu^{3+}$, yTm^{3+}, zTb^{3+}) samples. Gap energy values (*Egap*) were estimated by converting the reflectance data of the samples to absorbance using the Kubelka-Munk function [38] followed by the Wood and Tauc method [39]. The optical gap energy is given by $ahv \propto (hv\text{-}E_{gap})^k$ [39], where *h* is the Planck constant, *v* is the frequency, *a* is the absorbance and *k* is indicated for the different transitions. Regarding the $Sr_{0.9-x-y-z}Ca_{0.1}In_2O_4$ samples, $k = 2$ was implemented, which indicates a permitted indirect electronic transition. The graphs were plotted with absorbance versus photon energy (eV) and extrapolating the linear portion of the curve to zero absorption to estimate *Egap*. The estimated band gap values of the samples are approximate values to those found in the literature, as shown in Table 4.

It is observed that the gap energy of $Sr_{0.9-x-y-z}Ca_{0.1}In_2O_4$ samples tends to decrease as the substitutions of Sr^{2+} ions by an increase of Eu^{3+}, Tb^{3+} and Tb^{3+} ions, with this decrease being more significant with the increase in doping concentration of the Tb^{3+} ions. The increase in Eu^{3+} dopant concentration resulted in a slight increase in the gap energy, as this non-linear gap energy behavior with Eu^{3+} doping is reported in the literature with other materials. Gurgel et al [42] synthesized $PbMoO_4$:(Eu^{3+}, Tb^{3+}, Tm^{3+}) by the sonochemical method and observed non-linearity in the gap energy as the of Eu^{3+} doping increased (doping between 0.5% and 1.5 mol%). Lovisa et al [17] obtained $ZnMoO_4$:(Eu^{3+}, Tb^{3+}, Tm^{3+}) by the sonochemical method and observed similar behavior, with an increase and decrease in gap energy with the increase of Eu^{3+} doping (doping between 1% and 3 mol%). The changes in the gap energy of the samples occur due to the structural distortions, defects and load imbalance caused by the substitution of Sr^{2+} ions by RE^{3+} ions, which will introduce impurities and

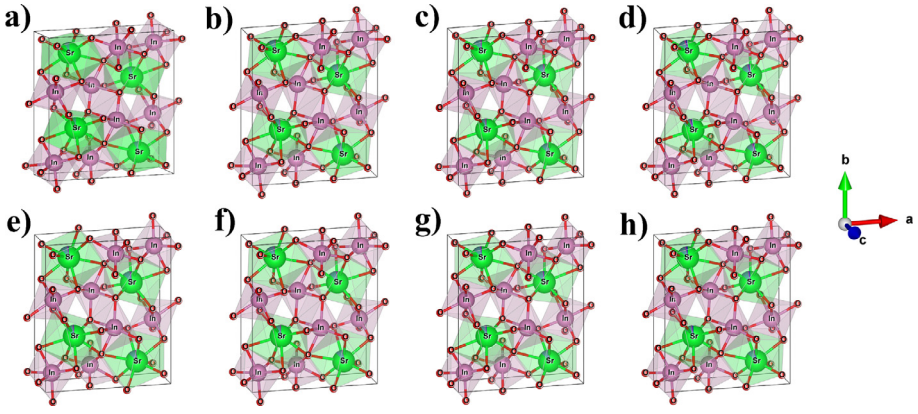

Fig. 3. Model of orthorhombic structure of the $Sr_{0.9-x-y-z}Ca_{0.1}In_2O_4$ obtained by USP (a) SCIO, (b) SCIO-1.0RE, (c) SCIO-1.5Eu, (d) SCIO-2.0Eu, (e) SCIO-1.5Tb, (f) SCIO-2.0Tb, (g) SCIO-1.5Tm and (h) SCIO-2.0Tm.

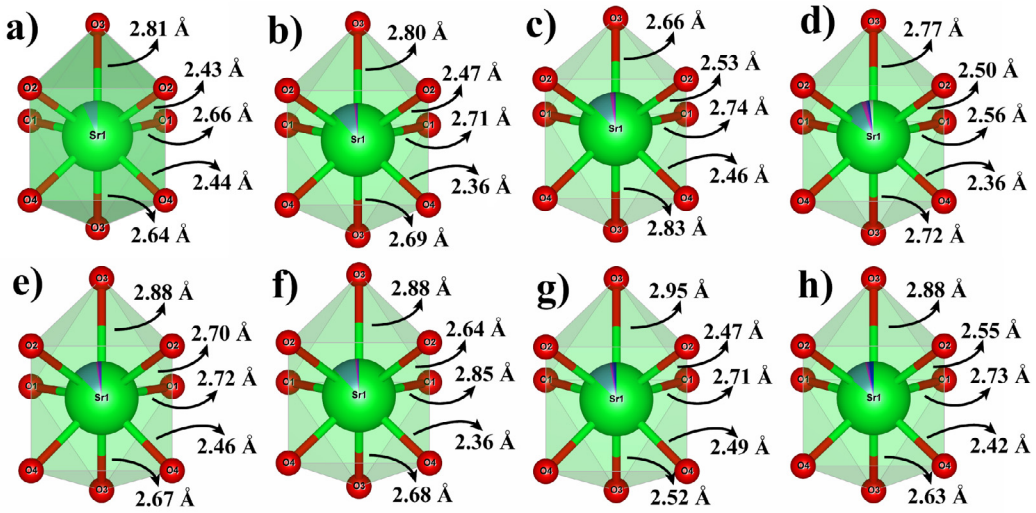

Fig. 4. Distances of the chemical bonds between Sr-O/Ca-O/RE-O atoms (a) SCIO, (b) SCIO-1.0RE, (c) SCIO-1.5Eu, (d) SCIO-2.0Eu, (e) SCIO-1.5Tb, (f) SCIO-2.0Tb, (g) SCIO-1.5Tm and (h) SCIO-2.0Tm.

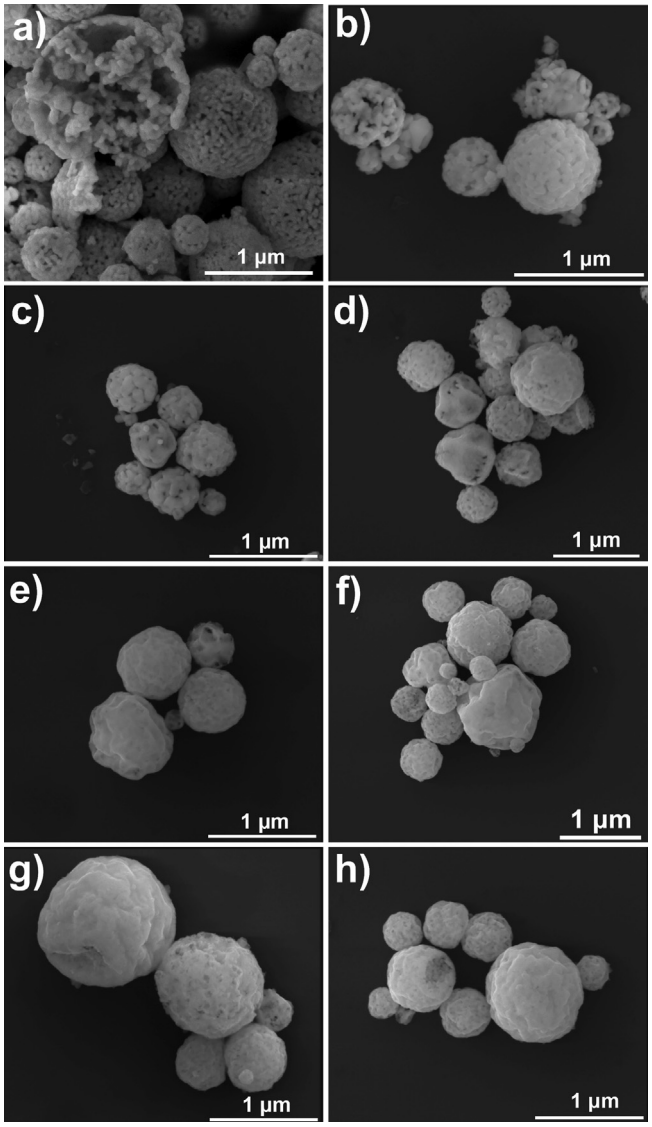

Fig. 5. SEM micrographs of (a) SCIO, (b) SCIO-1.0RE, (c) SCIO-1.5Eu, (d) SCIO-2.0Eu, (e) SCIO-1.5Tb, (f) SCIO-2.0Tb, (g) SCIO-1.5Tm and (h) SCIO-2.0Tm.

intermediate levels between the valence band and the conduction band of the samples [43–45].

3.4. Photoluminescence measurements

3.4.1. PL emission spectra $Sr_{0.9-x-y-z}Ca_{0.1}In_2O_4$:($xEu^{3+}$, yTm^{3+}, zTb^{3+} mol%) and quenching effect

Fig. 7 illustrates the photoluminescence emission profiles of the $Sr_{0.9-x-y-z}Ca_{0.1}In_2O_4$:($xEu^{3+}$, yTm^{3+}, zTb^{3+} mol%) particles. The samples were excited at 350.7 nm at room temperature. Luminescence spectra presented emission bands attributed to Tm^{3+}, $^5D_2 \rightarrow {}^3F_4$ and $^1G_4 \rightarrow {}^3H_6$ in 456 and 479 nm [46], accompanied by emissions of Tb^{3+}, $^5D_3 \rightarrow {}^7F_J$ (J = 6, 5, 3) in 417, 445 and 469 nm, $^5D_4 \rightarrow {}^7F_J$ (J = 6, 5) in 494 and 541 nm [47], and Eu^{3+}, $^5D_0 \rightarrow {}^7F_J$ (J = 1, 2, 3, 4) in 592, 621, 651 and 703 nm [48]. It is observed that the positions of the transition bands are the same, but their intensity varies according to the changes in the composition of the dopants (Eu^{3+}, Tm^{3+}, Tb^{3+}). The presence of a wide band comprised in the blue region with its maximum around 450 nm is also noticed for the SCIO-*x*%Eu and SCIO-*y*%Tm samples. The wide band for the SCIO-*z*%Tb samples undergoes a shift towards the green region with maximum around 550 nm due to the influence of the increase in Tb^{3+} concentration. The existence of this band width in the emission spectra is associated to the contribution of the SCIO matrix in the photoluminescent behavior. According to Medeiros et al [27], the broadband profile is related to relaxation by multiphonic and multilevel processes. This type of relaxation can happen through several paths and involves the participation of numerous intermediary states in the band gap. This change in band width is attributed to the positioning of network defects (i.e., oxygen vacancies, impurities, distorted links) in the band gap. Thus, the emission in blue-green is associated with an orderly structure with surface defects, while the red-yellow emission is associated with a disordered structure with deep defects [49].

For the SCIO-*x*%Eu samples presented in Fig. 7(a), the increase in the Eu^{3+} amount favored the increase of the emission intensity, increasing the luminescence. A decrease in the photoluminescence intensity is observed for the SCIO-2.0Tm and SCIO-2.0Tb samples. This behavior is well referenced in several works [50–52], and is known as the concentration quenching effect [53]. This behavior is associated to the cross-relaxation energy transfer between RE ions which are very close at a distance determined as critical distance (CD). In this condition, the activating ions (A) which are constituted by RE ions interact with each other so that non-radiative transitions are favored due to better non-radiative coupling between the ions [54]. The excitation

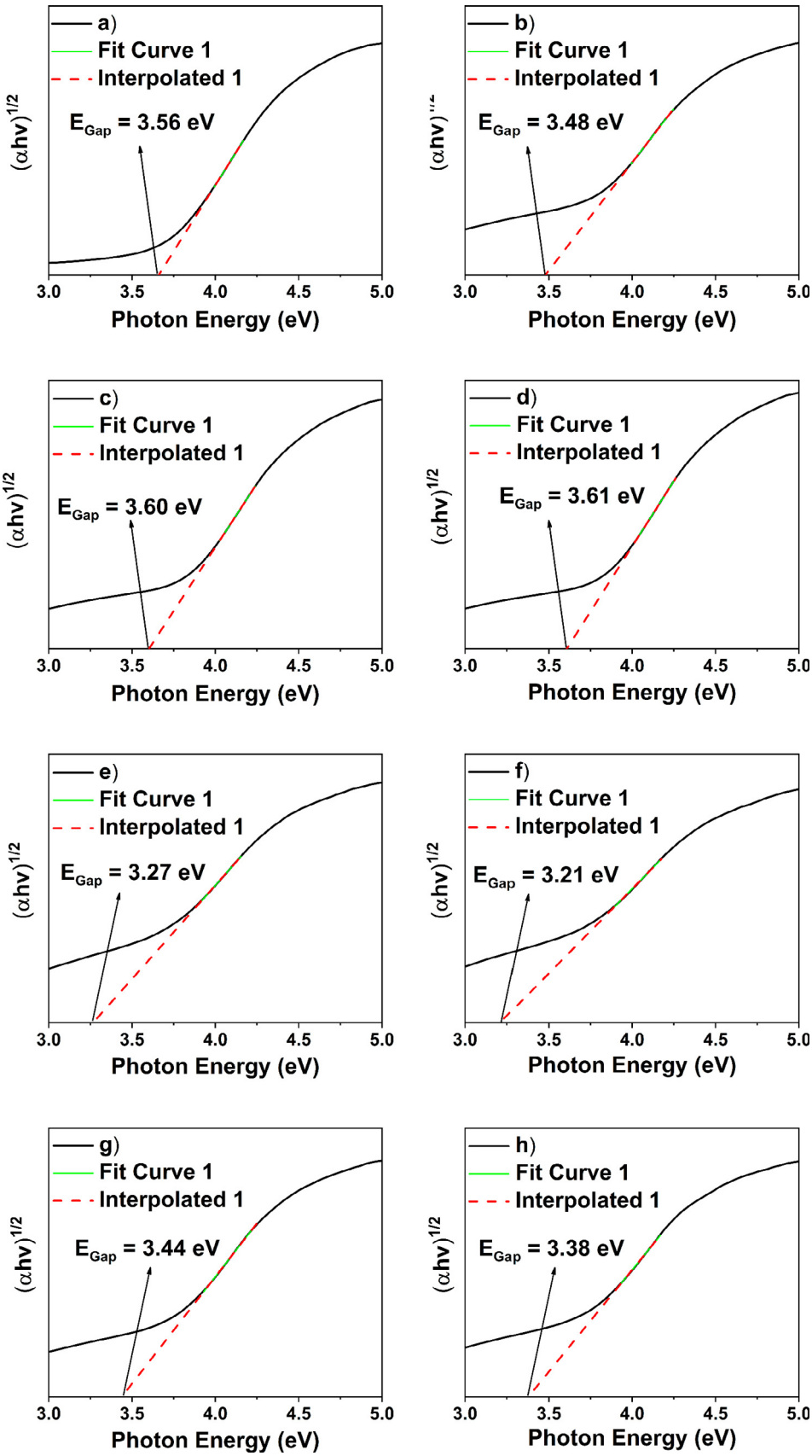

Fig. 6. UV–Vis absorbance spectra of (a) SCIO, (b) SCIO-1.0RE, (c) SCIO-1.5Eu, (d) SCIO-2.0Eu, (e) SCIO-1.5Tb, (f) SCIO-2.0Tb, (g) SCIO-1.5Tm and (h) SCIO-2.0Tm.

Table 4
Comparative results between the E_{gap} values of $Sr_{0.9-x-y-z}Ca_{0.1}In_2O_4$:($xEu^{3+}$, yTm^{3+}, zTb^{3+}) obtained in this work and those reported in the literature.

Sample	E_{gap} (eV)	Synthesis Method	Ref.
SCIO	3.56	USP	[This work]
SCIO-1.0RE	3.48	USP	[This work]
SCIO-1.5Eu	3.60	USP	[This work]
SCIO-2.0Eu	3.61	USP	[This work]
SCIO-1.5Tb	3.27	USP	[This work]
SCIO-2.0Tb	3.21	USP	[This work]
SCIO-1.5Tm	3.44	USP	[This work]
SCIO-2.0Tm	3.38	USP	[This work]
$SrIn_2O_4$	3.60	State Solid	[40]
$SrIn_2O_4$	3.66	Combustion	[41]

energy is transferred randomly from one ion to another, leading to the concentration quenching and consequently suppression in photoluminescence. According to Blasse, the CD can be expressed as [55]:

$$CD \cong 2\left(\frac{3V}{4X_c\pi Z}\right)^{1/3} \quad (2)$$

where V is the volume of the unit cell, X_c is the critical concentration of dopant ions, and Z is the number of the host cations in the unit cell. The following values for the SCIO-2.0Tm and SCIO-2.0Tb systems were considered: Z = 4, V(2%Tm) = 373.22 Å^3, V(2%Tb) = 374.04 Å^3 and X_c = 0.04. The calculated CD (2%Tm) and CD (2%Tb) values were 16.45 and 16.47 Å, respectively. Simple exchange interactions are promoted when the critical distance is within the 5–10 Å range [56]. In this case, other multipolar electrical interactions are responsible for the quenching effect for larger CDs. According to Dexter's theory there are three multipole-multipole interactions: dipole–dipole, dipole-quadrupole and quadrupole–quadrupole, respectively [57]. The RE-RE distance in the present work is larger than 10 Å. Accordingly, the interactions acting on the systems are calculated as the multipolar type.

3.4.2. Energy transfer in $Sr_{0.9-x-y-z}Ca_{0.1}In_2O_4$:($xEu^{3+}$, yTm^{3+}, zTb^{3+} mol%).

The present study aimed to investigate the possible energy transfer (ETs) between the ions in the triple doped samples. Tm^{3+} shows strong fluorescence in the blue region; in contrast, Tb^{3+} and Eu^{3+} ions have strong uptake in the blue region [54]. Therefore, the samples coded with the Tm^{3+}, Tb^{3+} and Eu^{3+} ions present great possibilities of the existence of ETs between ions due to their particular absorption and emission characteristics. Considering that the Tm^{3+}, Tb^{3+} and Eu^{3+} ions emit their characteristic colors in blue, green and red, respectively, then these dopants have potential white emission conditions when they are set at an appropriate concentration in a given matrix. Fig. 8 shows the diagram of energy levels of the rare earth ions used and the possible electronic transitions and energy transfers.

For the excitation of 350.7 nm, the Tm^{3+} ions in the fundamental state are promoted to state $^1D_2$, from which these ions decay radioactively to the $^3F_4$ state by emitting photons in the blue region. At the same time, Tm^{3+} ions relax non-radioactively from $^1D_2$ state to $^1G_4$ state, filling it. As time progresses, the meta-stable state of $^1G_4$ becomes depopulated and the Tm^{3+} ions relax to the ground state of $^3H_6$, emitting fluorescence. The Tm^{3+} ions are classified as sensitizers because they have higher absorption energy levels, being able to transfer part of this energy to the activating ions (Tb^{3+}, Eu^{3+}).

(i) ET1 refers to Tm^{3+} ($^1G_4$) → Tb^{3+} ($^5D_4$). When the Tm^{3+} ions excited in the $^1D_2$ state decay, part of their energy passes to the $^3F_4$ state emitting in blue, and another non-radioactively part decays

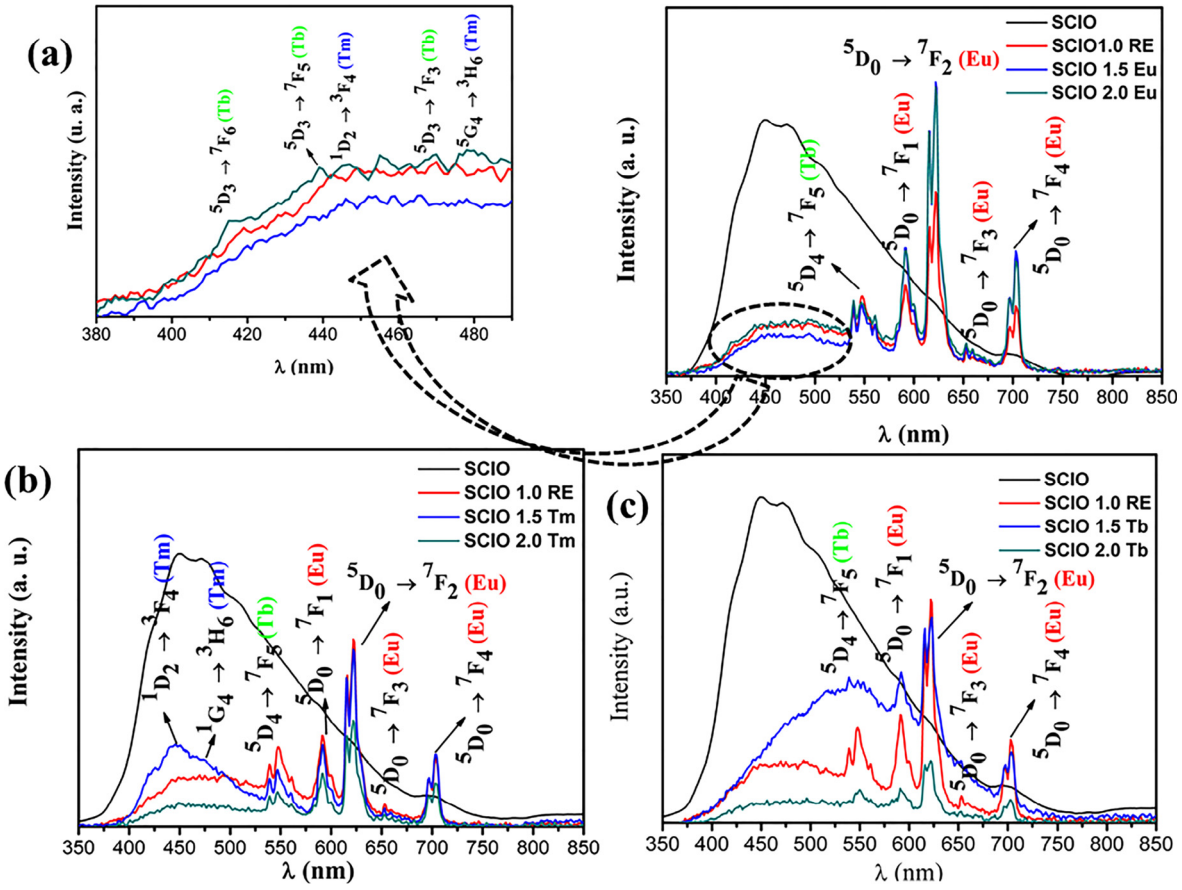

Fig. 7. Photoluminescence emission spectra: (a) SCIO-*x*%Eu, (b) SCIO-*y*%Tm and (c) SCIO-*z*%Tb, excited at 350.7 nm.

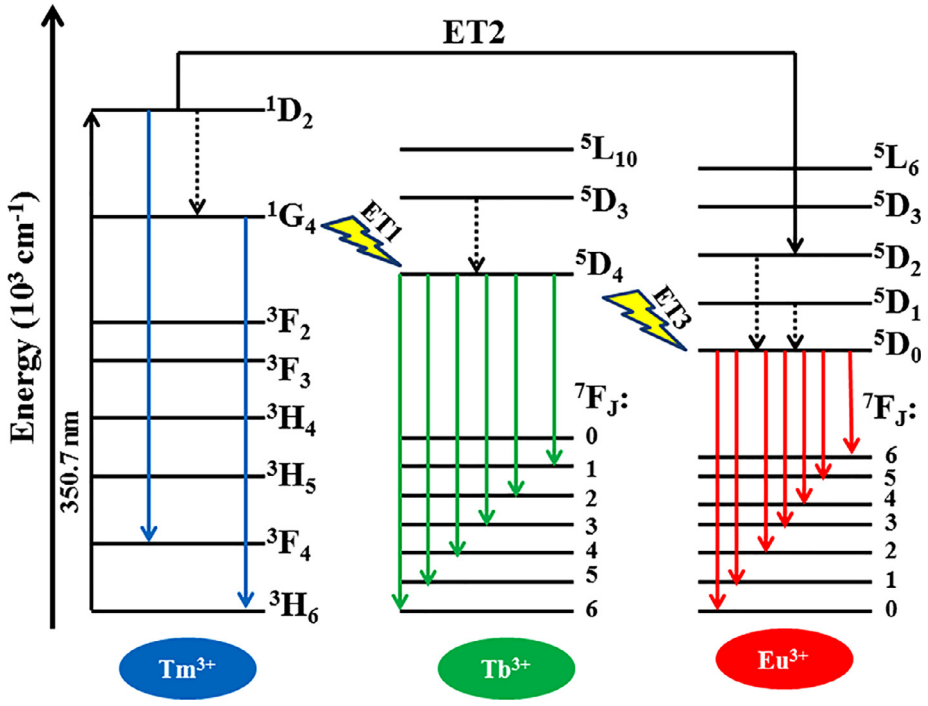

Fig. 8. Diagram of energy levels and the electronic transitions of Tm^{3+}, Tb^{3+} and Eu^{3+}.

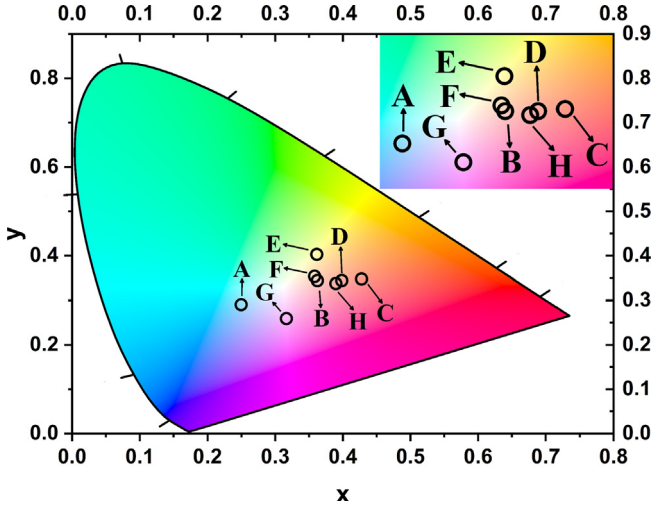

Fig. 9. CIE diagram of $Sr_{0.9-x-y-z}Ca_{0.1}In_2O_4$:($xEu^{3+}$, yTm^{3+}, zTb^{3+}).

to the metastable $^1G_4$ state, at the same time part of this energy is transferred to the $^5D_4$ state of Tb^{3+} [58].

(ii) ET2 refers to Tm^{3+} ($^1G_4$) → Eu^{3+} ($^5D_2$). The Tm^{3+} ions in the fundamental state are promoted to excited $^1D_2$ state which decomposes non-radioactively in the metastable state of $^1G_4$. The Tm^{3+} ions then directly transfer some of their energy to the $^5D_2$ state of Eu^{3+} during this process. Another type of energy migration is part of the $^1G_4$ (Tm^{3+}) state which subsequently transfers energy to the $^5D_2$ state of Eu^{3+} through the $^5D_4$ state of Tb^{3+} by means of non-radioactive relaxations. In this case, the presence of the Tb^{3+} ions facilitate ET2 between the Tm^{3+} and Eu^{3+} ions. The excited Eu^{3+} ions relax non-radioactively to $^5D_1$ and then to the metastable $^5D_0$ state. Therefore, these ions finally decay in a radioactive pathway from the metastable state to ^7F_J (J = 1, 2, 3 and 4) ground state by emitting photons in their respective regions [59].

(iii) ET3 refers to Tb^{3+} ($^5D_3$) → Eu^{3+} ($^5D_1$). The Tb^{3+} ions in the $^5D_3$ excited state non-radioactively relax at $^5D_4$ in the energy transfer process, and then transfer part of their energy to the $^5D_1$ excited state of Eu^{3+}. Eu^{3+} ions decay rapidly in a cascade effect through non-radioactive emission transitions filling the metastable state $^5D_0$. They subsequently relax radioactively by presenting their respective energy levels ^7F_J (J = 1, 2, 3 and 4) within the visible region [60].

3.4.3. *Color properties of $Sr_{0.9-x-y-z}Ca_{0.1}In_2O_4$:($xEu^{3+}$, yTm^{3+}, zTb^{3+} mol%).*

The chromaticity coordinates (*x*, *y*) of $Sr_{0.9-x-y-z}Ca_{0.1}In_2O_4$ samples are shown in Fig. 9. The luminescent color with the change in RE concentration may be visibly adequate and controlled. All samples emitted in the white region as shown in the chromaticity diagram. The

Table 5
Chromaticity coordinates (CIE) and correlated temperature color (CCT) for $Sr_{0.9-x-y-z}Ca_{0.1}In_2O_4$:($xEu^{3+}$, yTm^{3+}, zTb^{3+}).

Code	Sample	x	y	CCT (K)	CRI (%)	Color
A	SCIO	0.25	0.29	14108	83	Beginning dusk (Blue)
B	SCIO-1.0RE	0.36	0.34	4322	89	Neutral white
C	SCIO-1.5Eu	0.42	0.34	2655	79	Warm white (bulb)
D	SCIO-2.0Eu	0.39	0.34	3228	80	Warm white (bright halo)
E	SCIO-1.5Tb	0.36	0.40	4673	88	Between neutral white and daylight
F	SCIO-2.0 Tb	0.36	0.35	4530	95	Between neutral white and daylight
G	SCIO-1.5Tm	0.32	0.26	7205	59	Light summer shade
H	SCIO-2.0Tm	0.38	0.34	3385	84	Between warm white and neutral white

correlated color temperatures (CCTs) exhibit a variation between the values of 2655–7205 K for samples doped with RE^{3+}. The Color Reproducibility Index (CRI) was also evaluated and all samples presented values equal to or greater than 80%, except for the SCIO-1.5%Tm sample with 59%. This result represents that the light emitted by the samples faithfully reproduce the colors seen in the objects, independent of the CCT values. The adjustable luminescent properties of $Sr_{0.9-x-y-z}Ca_{0.1}In_2O_4$:($xEu^{3+}$, yTm^{3+}, zTb^{3+} mol%) which were investigated prove their potential application in the LED display devices. Table 5 records all information regarding the color characteristics of $Sr_{0.9-x-y-z}Ca_{0.1}In_2O_4$:($xEu^{3+}$, yTm^{3+}, zTb^{3+} mol%) according to the behavior shown in the emission spectra in Fig. 7.

4. Conclusion

The $Sr_{0.9-x-y-z}Ca_{0.1}In_2O_4$ particles were successfully obtained by the USP method. In observing the XRD results, it was possible to identify the formation of the orthorhombic phase without the presence of the secondary phase, indicating that the dopants were successfully introduced into the matrix. The morphology of the $Sr_{0.9-x-y-z}Ca_{0.1}In_2O_4$ particles is spherical with small distortions presenting a level of surface porosity, with the morphology of the pure sample having a spongy shape, whereas the doped samples with higher rare earth content have a deflated ball-shape microsphere. The gap energy was estimated between 3.21 and 3.66 eV, and this variation may be associated with the defects, structural distortions and imbalance of loads caused by the substitution: $Sr^{2+} \rightarrow RE^{3+}$. The photoluminescence results present well-defined Eu^{3+}, Tm^{3+} and Tb^{3} emissions and an expressive contribution of the SCIO matrix. All samples showed emission in white and the majority had CRI ≥ 80%.

Acknowledgment

The authors thank the following Brazilian research financing institutions for financial support: A.A.G. Santiago acknowledge financial support from National Council for Scientific and Technological Development – CNPq. São Paulo Research Foundation - FAPESP (Brazil) (Processo 2013/07296-2), (2016/23891-6). Coordination for the Improvement of Higher Education Personnel (CAPES) - Brazil (CAPES) - Finance Code 001 and CAPES/PROCAD 2013/2998/2014 and Graduate Program in Materials Science and Engineering (PPGCEM-UFRN).

Appendix A. Supplementary data

Supplementary data to this article can be found online at https://doi.org/10.1016/j.ultsonch.2019.03.028.

References

[1] X. Liu, T. Li, X. Zhao, H. Suo, Z. Zhang, P. Zhao, S. Gao, M. Niu, 808 nm-triggered optical thermometry based on up-conversion luminescence of $Nd^{3+}/Yb^{3+}/Er^{3+}$ doped MIn_2O_4 (M = Ca, Sr and Ba) phosphors, Dalton Trans. 47 (2018) 6713–6721.
[2] Y. Kang, B. Thuy, Y. Shimokawa, T. Hayakawa, S. Sakaida, L. Miao, S. Tanemura, S. Honda, Y. Iwamoto, Relationship between Eu3+ substitution sites and photoluminescence properties of $SrIn_2O_4$:Eu^{3+} spinel phosphors, J. Lumin. 169 (2016) 78–85.
[3] S.B. Kokane, S.D. Sartale, C.A. Betty, R. Sasikala, Pd–TiO_2–$SrIn_2O_4$ heterojunction photocatalyst: enhanced photocatalytic activity for hydrogen generation and degradation of methylene blue, RSC Adv. 4 (2014) 55539–55547.
[4] J. Tang, Z. Zou, M. Katagiri, T. Kako, J. Ye, Photocatalytic degradation of MB on MIn_2O_4 (M= alkali earth metal) under visible light: effects of crystal and electronic structure on the photocatalytic activity, Catal. Today 93 (2004) 885–889.
[5] J. Tang, Z. Zou, J. Ye, Effects of substituting Sr^{2+} and Ba^{2+} for Ca^{2+} on the structural properties and photocatalytic behaviors of $CaIn_2O_4$, Chem. Mater. 16 (2004) 1644–1649.
[6] A. Baszczuk, M. Jasiorski, M. Nyk, J. Hanuza, M. Mączka, W. Stręk, Luminescence properties of europium activated $SrIn_2O_4$, J. Alloys Compd. 394 (2005) 88–92.
[7] R.v. Schenck, H. Müller-buschbaum, Über Erdalkalimetalloxoindate. III. Kristallstrukturuntersuchung an $SrIn_2O_4$, Zeitschrift für anorganische und allgemeine, Chemie 398 (1973) 24–30.
[8] M. Guan, H. Zheng, L. Mei, M.S. Molokeev, J. Xie, T. Yang, X. Wu, S. Huang, Z. Huang, Preparation, structure, and up-conversion luminescence of Yb^{3+}/Er^{3+} codoped $SrIn_2O_4$ phosphors, J. Am. Ceram. Soc. 98 (2015) 1182–1187.
[9] X. Yan, W. Li, K. Sun, A novel red emitting phosphor $CaIn_2O_4$: Eu^{3+}, Sm^{3+} with a broadened near-ultraviolet absorption band for solid-state lighting, Mater. Res. Bull. 46 (2011) 87–91.
[10] T. Li, C. Guo, L. Li, Up-conversion luminescence of Er^{3+}-Yb^{3+} co-doped $CaIn_2O_4$, Opt. Express 21 (2013) 18281–18289.
[11] M. Guan, H. Zheng, L. Mei, Z. Huang, T. Yang, M. Fang, Y. Liu, Infrared-to-visible up-conversion luminescence and energy transfer of RE^{3+}/Yb^{3+} (RE= Ho, Tm) co-doped $SrIn_2O_4$, Infrared Phys. Technol. 67 (2014) 107–110.
[12] H. Wang, L. Tian, Luminescence properties of $SrIn_2O_4$: Eu^{3+} incorporated with Gd^{3+} or Sm^{3+} ions, J. Alloys Compd. 509 (2011) 2659–2662.
[13] X. Liu, C. Lin, Y. Luo, J. Lin, Host-sensitized luminescence of Dy^{3+}, Pr^{3+}, Tb^{3+} in polycrystalline $SrIn_2O_4$ for field emission displays, J. Electrochem. Soc. 154 (2007) J21–J27.
[14] Z. Ci, Q. Sun, S. Qin, M. Sun, X. Jiang, X. Zhang, Y. Wang, Warm white light generation from a single phase Dy^{3+} doped $Mg_2Al_4Si_5O_{18}$ phosphor for white UV-LEDs, PCCP 16 (2014) 11597–11602.
[15] A. Gupta, N. Brahme, D. Prasad Bisen, Electroluminescence and photoluminescence of rare earth (Eu, Tb) doped Y_2O_3 nanophosphor, J. Lumin. 155 (2014) 112–118.
[16] G. Alarcón-Flores, M. García-Hipólito, M. Aguilar-Frutis, S. Carmona-Téllez, R. Martinez-Martinez, M.P. Campos-Arias, E. Zaleta-Alejandre, C. Falcony, Synthesis and fabrication of Y_2O_3:Tb^{3+} and Y_2O_3:Eu^{3+} thin films for electroluminescent applications: optical and structural characteristics, Mater. Chem. Phys. 149–150 (2015) 34–42.
[17] L.X. Lovisa, M.C. Oliveira, J. Andrés, L. Gracia, M.S. Li, E. Longo, R.L. Tranquilin, C.A. Paskocimas, M.R.D. Bomio, F.V. Motta, Structure, morphology and photoluminescence emissions of $ZnMoO_4$: RE^{3+} = Tb^{3+}-Tm^{3+}-X Eu^{3+} (x = 1, 1.5, 2, 2.5 and 3 mol%) particles obtained by the sonochemical method, J. Alloys Compd. 750 (2018) 55–70.
[18] L.X. Lovisa, J. Andrés, L. Gracia, M.S. Li, C.A. Paskocimas, M.R.D. Bomio, V.D. Araujo, E. Longo, F.V. Motta, Photoluminescent properties of ZrO_2: Tm^{3+}, Tb^{3+}, Eu^{3+} powders—a combined experimental and theoretical study, J. Alloy. Compd. 695 (2017) 3094–3103.
[19] Y.-C. Lin, M. Karlsson, M. Bettinelli, Inorganic phosphor materials for lighting, in: N. Armaroli, H.J. Bolink (Eds.), Photoluminescent Materials and Electroluminescent Devices, Springer International Publishing, Cham, 2017, pp. 309–355.
[20] G. García-Rosales, F. Mercier-Bion, R. Drot, G. Lagarde, J. Roques, E. Simoni, Energy transfer from Tb^{3+} to Eu^{3+} ions sorbed on $SrTiO_3$ surface, J. Lumin. 132 (2012) 1299–1306.
[21] M. Fhoula, T. Kallel, M. Messaoud, M. Dammak, E. Cavalli, Morphological, spectroscopic and photocatalytic properties of Eu^{3+}:TiO_2 synthesized by solid-state and hydrothermal-assisted sol-gel processes, Ceram. Int. 45 (2019) 3675–3679.
[22] J. Zhang, R. Li, L. Liu, L. Li, L. Zou, S. Gan, G. Ji, Self-assembled 3D sphere-like $SrMoO_4$ and SrMoO4:Ln^{3+} (Ln = Eu, Sm, Tb, Dy) microarchitectures: facile sonochemical synthesis and optical properties, Ultrason. Sonochem. 21 (2014) 1736–1744.
[23] M. Zhao, Y. Liu, S. Ma, D. Liu, K. Wang, Investigation of energy transfer mechanism and luminescence properties in Eu^{3+} and Sm^{3+} co-doped $ZnWO_4$ phosphors, J. Lumin. 202 (2018) 57–64.
[24] C.R.R. Almeida, L.X. Lovisa, A.A.G. Santiago, M.S. Li, E. Longo, C.A. Paskocimas, F.V. Motta, M.R.D. Bomio, One-step synthesis of $CaMoO_4$: Eu^{3+} nanospheres by ultrasonic spray pyrolysis, J. Mater. Sci.: Mater. Electron. 28 (2017) 16867–16879.
[25] V. Jokanović, B. Čolović, M. Dutour Sikirić, V. Trajković, A new approach to the drug release kinetics of a discrete system: SiO_2 system obtained by ultrasonic dry spraying, Ultrason. Sonochem. 20 (2013) 535–545.
[26] V. Jokanovic, Z. Nedic, Nano-designing of Mg doped phosphate tungsten bronzes and SiO_2 composite obtained by ultrasonic spray pyrolysis method, Ultrason. Sonochem. 17 (2010) 228–233.
[27] P.N. Medeiros, A.A.G. Santiago, E.A.C. Ferreira, M.S. Li, E. Longo, M.R.D. Bomio, F.V. Motta, Influence Ca-doped $SrIn_2O_4$ powders on photoluminescence property prepared one step by ultrasonic spray pyrolysis, J. Alloys Compd. 747 (2018) 1078–1087.
[28] A.A.G. Santiago, C.R.R. Almeida, R.L. Tranquilin, R.M. Nascimento, C.A. Paskocimas, E. Longo, F.V. Motta, M.R.D. Bomio, Photoluminescent properties of the $Ba_{1-x}Zn_xMoO_4$ heterostructure obtained by ultrasonic spray pyrolysis, Ceram. Int. 44 (2018) 3775–3786.
[29] H. Rietveld, A profile refinement method for nuclear and magnetic structures, J. Appl. Crystallogr. 2 (1969) 65–71.
[30] B. Toby, EXPGUI, a graphical user interface for GSAS, J. Appl. Crystallogr. 34 (2001) 210–213.
[31] G. Ming, Z. Hong, M. Lefu, M.S. Maxim, X. Jing, Y. Tao, W. Xiaowen, H. Saifang, H. Zhaohui, Preparation, structure, and up-conversion luminescence of Yb^{3+}/Er^{3+} codoped $SrIn_2O_4$ phosphors, J. Am. Ceram. Soc. 98 (2015) 1182–1187.
[32] R. Shannon, Revised effective ionic radii and systematic studies of interatomic distances in halides and chalcogenides, Acta Crystallogr. Sect. A 32 (1976) 751–767.
[33] B. Wu, W. Yang, H. Liu, L. Huang, B. Zhao, C. Wang, G. Xu, Y. Lin, Fluorescence spectra and crystal field analysis of $BaMoO_4$: Eu^{3+} phosphors for white light-emitting diodes, Spectrochim. Acta Part A: Mol. Biomol. Spectrosc. 123 (2014) 12–17.
[34] L. Lv, J. Wang, W. Wang, L. Han, Microstructure control by Y^{3+} ions doping in $CaMoO_4$:Eu^{3+}: tunable optical and luminescent performance, J. Alloys Compd. 635 (2015) 25–33.

[35] S. Bishop, D. Marrocchelli, W. Fang, K. Amezawa, K. Yashiro, G. Watson, Reducing the chemical expansion coefficient in ceria by addition of zirconia, Energy Environ. Sci. 6 (2013) 1142–1146.
[36] K. Momma, F. Izumi, VESTA 3 for three-dimensional visualization of crystal, volumetric and morphology data, J. Appl. Crystallogr. 44 (2011) 1272–1276.
[37] G.L. Messing, S.-C. Zhang, G.V. Jayanthi, Ceramic powder synthesis by spray pyrolysis, J. Am. Ceram. Soc. 76 (1993) 2707–2726.
[38] L. Tolvaj, K. Mitsui, D. Varga, Validity limits of Kubelka-Munk theory for DRIFT spectra of photodegraded solid wood, Wood Sci. Technol. 45 (2011) 135–146.
[39] D.L. Wood, J. Tauc, Weak absorption tails in amorphous semiconductors, Phys. Rev. B 5 (1972) 3144–3151.
[40] S. Esther Dali, V.V.S.S. Sai Sundar, M. Jayachandran, M.J. Chockalingam, Synthesis and characterization of Aln_2O_4 indates, A = Mg, Ca, Sr, Ba, J. Mater. Sci. Lett. 17 (1998) 619–623.
[41] S.B. Kokane, S. Sartale, C. Betty, R. Sasikala, Pd–TiO_2–$SrIn_2O_4$ heterojunction photocatalyst: enhanced photocatalytic activity for hydrogen generation and degradation of methylene blue, RSC Adv. 4 (2014) 55539–55547.
[42] G.M. Gurgel, L.X. Lovisa, L.M. Pereira, F.V. Motta, M.S. Li, E. Longo, C.A. Paskocimas, M.R.D. Bomio, Photoluminescence properties of (Eu, Tb, Tm) co-doped $PbMoO_4$ obtained by sonochemical synthesis, J. Alloys Compd. 700 (2017) 130–137.
[43] C. Regmi, Y.K. Kshetri, S.K. Ray, R.P. Pandey, S.W. Lee, Utilization of visible to NIR light energy by Yb^{+3}, Er^{+3} and Tm^{+3} doped $BiVO_4$ for the photocatalytic degradation of methylene blue, Appl. Surf. Sci. 392 (2017) 61–70.
[44] G. Sanal Kumar, N. Illyaskutty, S. Suresh, R.S. Sreedharan, V.U. Nayar, V.P.M. Pillai, Terbium oxide doped MoO_3 nanostructures: morphology engineering and enhanced photoluminescence, J. Alloys Compd. 698 (2017) 215–227.
[45] B.-G. Zhai, Y.M. Huang, Green photoluminescence and afterglow of Tb-doped $SrAl_2O_4$, J. Mater. Sci. 52 (2017) 1813–1822.
[46] L. Cai, L. Ying, J. Zheng, B. Fan, R. Chen, C. Chen, Luminescent properties of $Sr_2B_2O_5$: Tm^{3+}, Na^+ blue phosphor, Ceram. Int. 40 (2014) 6913–6918.
[47] V. Singh, K. Shinde, M. Pathak, N. Singh, V. Dubey, P.K. Singh, H. Jirimali, Green emission from Tb^{3+}-doped $CaLaAl_3O_7$ phosphor–a photoluminescence study, Optik 164 (2018) 407–413.
[48] D. Kumar, B. Singh, M. Srivastava, A. Srivastava, S. Srivastava, Structural and photoluminescence properties of thermally stable Eu^{3+} activated $CaWO_4$ nanophosphor via Li^+ incorporation, J. Lumin. (2018).
[49] A.P.A. Marques, F.V. Motta, M.A. Cruz, J.A. Varela, E. Longo, I.L. Rosa, $BaMoO_4$: Tb^{3+} phosphor properties: synthesis, characterization and photophysical studies, Solid State Ionics 202 (2011) 54–59.
[50] T.T.T. Chanu, N. Rajmuhon Singh, Investigation on optical band gap, photoluminescence properties and concentration quenching mechanism of $Pb_{1-x}Tb_x^{3+}WO_4$ green-emitting phosphors, Spectrochim. Acta Part A: Mol. Biomol. Spectrosc. 191 (2018) 539–546.
[51] P. Jena, S.K. Gupta, V. Natarajan, M. Sahu, N. Satyanarayana, M. Venkateswarlu, Structural characterization and photoluminescence properties of sol–gel derived nanocrystalline $BaMoO_4$:Dy^{3+}, J. Lumin. 158 (2015) 203–210.
[52] O. Meza, E.G. Villabona-Leal, L.A. Diaz-Torres, H. Desirena, J.L. Rodríguez-López, E. Pérez, Luminescence concentration quenching mechanism in Gd_2O_3:Eu^{3+}, J. Phys. Chem. A 118 (2014) 1390–1396.
[53] J. McNamara, N. Albarakati, M. Reshchikov, Abrupt and tunable quenching of photoluminescence in ZnO, J. Lumin. 178 (2016) 301–306.
[54] V. Naresh, K. Gupta, C. Parthasaradhi Reddy, B.S. Ham, Energy transfer and colour tunability in UV light induced Tm^{3+}/Tb^{3+}/Eu^{3+}: ZnB glasses generating white light emission, Spectrochim. Acta Part A: Mol. Biomol. Spectrosc. 175 (2017) 43–50.
[55] G. Blasse, Energy transfer in oxidic phosphors, Philips Res. Rep. 24 (1969) 131.
[56] F. Kang, Y. Zhang, M. Peng, Controlling the energy transfer via multi luminescent centers to achieve white light/tunable emissions in a single-phased X2-type Y_2SiO_5: Eu^{3+}, Bi^{3+} phosphor for ultraviolet converted LEDs, Inorg. Chem. 54 (2015) 1462–1473.
[57] Y. Zhang, D. Geng, X. Li, J. Fan, K. Li, H. Lian, M. Shang, J. Lin, Wide-band excited $YTiTaO_6$: Eu^{3+}/Er^{3+} phosphors: structure refinement, luminescence properties, and energy transfer mechanisms, J. Phys. Chem. C 118 (2014) 17983–17991.
[58] B. Zhou, L. Tao, Y.H. Tsang, E.Y.-B. Pun, Broadband 1.20 μm emission in Tm^{3+}-doped and Tm^{3+}/Tb^{3+}, Eu^{3+} codoped gallogermanate glasses, Opt. Mater. 34 (2012) 1776–1780.
[59] S.-H. Yang, C.-H. Yen, C.-M. Lin, P.-J. Chiang, Energy transfer mechanism and luminescence properties of color tunable $LaPO_4$: Tm Eu phosphor, Ceram. Int. 41 (2015) 8211–8215.
[60] G.L. Reddy, L.R. Moorthy, T. Chengaiah, B. Jamalaiah, Multi-color emission tunability and energy transfer studies of $YAl_3(BO_3)_4$: Eu^{3+}/Tb^{3+} phosphors, Ceram. Int. 40 (2014) 3399–3410.